Monthly Notices
of the
ROYAL ASTRONOMICAL SOCIETY

Mon. Not. R. Astron. Soc. **426,** 2652–2667 (2012) doi:10.1111/j.1365-2966.2012.21543.x

The Keck Aperture Masking Experiment: dust-enshrouded red giants

T. D. Blasius,[1,2⋆] J. D. Monnier,[1] P. G. Tuthill,[3] W. C. Danchi[4] and M. Anderson[1]

[1]*Department of Astronomy, University of Michigan, Ann Arbor, MI 48109, USA*
[2]*Department of Physics, California Institute of Technology, Pasadena CA 91106, USA*
[3]*School of Physics, University of Sydney, Sydney, NSW 2006, Australia*
[4]*NASA-GSFC, 8800 Greenbelt Road, Greenbelt, MD 20771, USA*

Accepted 2012 June 18. Received 2012 June 7; in original form 2012 March 31

ABSTRACT

While the importance of dusty asymptotic giant branch (AGB) stars to galactic chemical enrichment is widely recognized, a sophisticated understanding of the dust formation and wind-driving mechanisms has proven elusive due in part to the difficulty in spatially resolving the dust-formation regions themselves. We have observed 20 dust-enshrouded AGB stars as part of the Keck Aperture Masking Experiment, resolving all of them in multiple near-infrared bands between 1.5 and 3.1 μm. We find 45 per cent of the targets to show measurable elongations that, when correcting for the greater distances of the targets, would correspond to significantly asymmetric dust shells at par with the well-known cases of IRC + 10216 or CIT 6. Using radiative transfer models, we find the sublimation temperature of $T_{\rm sub}$ (silicates) = 1130 ± 90 K and $T_{\rm sub}$ (amorphous carbon) = 1170 ± 60 K, both somewhat lower than expected from laboratory measurements and vastly below temperatures inferred from the inner edge of young stellar objects discs. The fact that O-rich and C-rich dust types showed the same sublimation temperature was surprising as well. For the most optically thick shells ($\tau_{2.2\,\mu{\rm m}} > 2$), the temperature profile of the inner dust shell is observed to change substantially, an effect we suggest could arise when individual dust clumps become optically thick at the highest mass-loss rates.

Key words: radiative transfer – instrumentation: interferometers – circumstellar matter.

1 INTRODUCTION

One of the most dramatic phases in the life of an intermediate mass star is the asymptotic giant branch (AGB), a relatively short period where a star loses most of its initial mass through a dusty wind. Researchers still do not understand all the ingredients necessary for producing the high mass-loss rates observed during this stage. The massive envelopes ejected during this phase are thought to be later illuminated during the planetary nebula stage, a stage where most stars show strong departure from spherical symmetry (Balick & Frank 2002).

Following the advent of infrared (IR) detectors, early workers made simple spherically symmetric models of dusty shells around large samples of AGB stars fitting only to the spectral energy distributions (e.g. Rowan-Robinson & Harris 1982, 1983a,b). M-type stars are typically surrounded by dust shells composed of amorphous silicates while C-stars have carbonaceous dust. These early workers were able to show that dust condensed around 1000 K within a few stellar radii of the stars and also estimated mass-loss rates typically $10^{-6}\,{\rm M}_\odot\,{\rm yr}^{-1}$ and as high as $10^{-4}\,{\rm M}_\odot\,{\rm yr}^{-1}$. More recently, Ivezic & Elitzur (1995) developed the code DUSTY to study dust shells in a systematic way and made models for a large sample of stars, again fitting just the spectral energy distribution.

The simple picture of spherically symmetric and uniform mass-loss was challenged by the observations of the Infrared Spatial Interferometer (ISI), a long-baseline mid-IR interferometer (Danchi et al. 1994). These workers found a diversity of shell morphologies with some red giants showing episodic dust shell ejections and others with a more continuous distribution of dust. This suggests dynamic and asymmetric mass-loss models fit into debates about the origins of aspherical symmetry in planetary nebulae. High angular resolution near-IR speckle and aperture masking on 8-m class telescopes were able to image fine details on some dust shells, such as the prototype carbon star IRC + 10216 (e.g. Haniff & Buscher 1998; Weigelt et al. 1998; Tuthill et al. 2000a). An elaborate model was presented by Men'shchikov, Hofmann & Weigelt (2002) arguing for complex, spatially varying dust properties and density structures. While IRC + 10216 shows complexity within the inner few stellar radii, it is unclear if these structures represent *global* asymmetries or just *weather conditions* of the dust formation process observed in situ.

Here we present the full data set of dust-enshrouded giants observed with the 10-yr project called the Keck Aperture Masking Experiment (Tuthill et al. 2000b). This experiment delivered well-calibrated spatial information on the scale of ∼50 milliarcseconds

⋆E-mail: tblasius@caltech.edu

Table 1. Properties of NIRC camera infrared filters. Reference: The NIRC Manual.

Name	Center wavelength λ_0 (μm)	Bandpass FWHM $\Delta\lambda$ (μm)	Fractional bandwidth (per cent)
FeII	1.6471	0.0176	1.1
H	1.6575	0.333	20
K	2.2135	0.427	19
Kcont	2.259 65	0.0531	2.3
CH4	2.269	0.155	6.8
PAHcs	3.0825	0.1007	3.3

(mas) in the astronomical K band ($\lambda_0 = 2.2\,\mu$m), which resolves all the dusty targets presented here well enough to measure their dust shell sizes and asymmetries, although the objects were not sufficiently resolved for reliable imaging. This paper includes 20 objects with observations in typically three wavelength ranges, 1.65, 2.2 and 3.1 μm. We have also extracted photometry to construct coeval near-IR spectral energy distributions – an important factor since these objects pulsate and show large variations in flux on yearly time-scales. Lastly, we used a radiative transfer code to fit each epoch of each target star using simultaneously the NRCR photometry and multi-wavelength angular size information from Keck masking.

The primary goals of these observations and modelling efforts are to measure the physical characteristics of a large sample of the most extreme dusty AGB stars, to address the question of the onset of circumstellar asymmetries, to determine any differences between silicate and carbon-rich dust shells, and to constrain the optical properties of the dust particles themselves. Lastly, this publication marks the final large data release of AGB star data from our diffraction-limited Keck masking experiment and we anticipate that this work will provide a rich data set for more detailed modelling efforts by other workers.

2 OBSERVATIONS

2.1 Overview of observations

Our observations consist of photometric and visibility data taken on 20 different stars at the W. M. Keck Observatory between 1997 December and 2002 July. The wavelengths at which these stars were observed and the properties of the corresponding filters are listed in Table 1. A listing of the observed stars, segregated into carbon-rich and oxygen-rich groups, along with their basic properties can be found in Table 2. Most stars were measured at more than one epoch during this time span allowing for robust internal data quality checks.

2.2 Photometric data

Aperture masking procedures consist of alternating target and calibrator observations that allow for basic photometry in most observing conditions. As part of the standard pipeline (Monnier 1999; Tuthill et al. 2000b), we performed aperture photometry on each object, allowing for the difference in magnitude (Δmag) between the target star and the calibrator star to be measured. The VizieR catalogue service, most often referencing the Catalogue of Infrared Observations (Gezari, Pitts & Schmitz 1993) and Two Micron All Sky Survey (2MASS) (Skrutskie et al. 2006), was used to determine magnitudes at IR wavelengths for the calibrators. Interpolation was used between wavelengths found in the catalogues and the wavelengths at which our data were

Table 2. Basic properties of targets.

Source names	RA (J2000) ($^{\rm h}$ $^{\rm m}$ $^{\rm s}$)	Dec. (J2000) ($^\circ$ $'$ $''$)	V (mag)	J^a (mag)	H^a (mag)	$K_{\rm s}{}^a$ (mag)	Spectral type
AFGL 230	01 33 51.21	+62 26 53.5	–	16.747	11.232	7.097	M[7]
AFGL 2019	17 53 18.9	−26 56 37	20.2[2]	6.338	4.035	2.616	M8[1]
AFGL 2199	18 35 46.48	+05 35 46.5	–	8.04	4.85	2.701	M[6]
AFGL 2290	18 58 30.02	+06 42 57.7	–	13.169	8.966	5.862	M[6]
CIT 1	00 06 52.94	+43 05 00.0	9.00[1]	3.041	1.829	1.115	M9[1]
CIT 3	01 06 25.98	+12 35 53.0	—	7.45	4.641	2.217	M9[1]
v1300 Aql	20 10 27.87	−06 16 13.6	20[1]	6.906	3.923	2.059	M[1]
AFGL 1922	17 07 58.24	−24 44 31.1	–	12.244	9.181	6.342	C[3]
AFGL 1977	17 31 54.98	+17 45 19.7	9.9[4]	10.536	7.994	5.607	C[1]
AFGL 2135	18 22 34.50	+27 06 30.2	–	9.043	6.002	3.643	C[1]
AFGL 2232	18 41 54.39	+17 41 08.5	9.7[1]	5.742	3.444	1.744	C[1]
AFGL 2513	20 09 14.22	+31 25 44.0	–	8.229	5.705	3.69	C[1]
AFGL 2686	20 59 08.88	+27 26 41.7	20[1]	9.112	6.268	4.075	Ce[1]
AFGL 4211	15 11 41.89	−48 20 01.3	–	10.711	7.751	5.154	C[3]
IRAS 15148−4940	15 18 22.05	−49 51 04.6	11.8[1]	5.297	3.071	1.696	C[1]
IY Hya	10 17 00.52	−14 39 31.4	14[1]	5.919	3.666	1.964	C[5]
LP And	23 34 27.66	+43 33 02.4	–	9.623	6.355	3.859	C[1]
RV Aqr	21 05 51.68	−00 12 40.3	11.5[1]	4.046	2.355	1.239	C[5]
v1899 Cyg	21 04 14.8	+53 21 03	15.6[1]	10.84	8.693	6.596	C8[5]
V Cyg	20 41 18.2702	+48 08 28.835	7.7[1]	3.096	1.273	0.117	C[1]

[a]These magnitudes (from 2MASS) are merely representative since the targets are variable. See Table 3 for our new photometry.

Note. The horizontal line separates oxygen rich (top) from carbon rich (bottom).

References: (1) SIMBAD, (2) Monet (1998), (3) Buscombe (1998), (4) Egret et al. (1992), (5) Skiff (2009), (6) Olnon (1986) – see also www.iras.ucalgary.ca/~volk/getlrs_plot.html, (7) Garcia-Hernandez et al. (2007).

Table 3. Journal of observations and derived photometry.

Target	Date(s) (UT)	Filter	Aperture mask	Magnitude	Calibrator names
AFGL 230	1997 December	k	FFA	8.34 ± 0.1	χ Cas
		PAHcs	KL relation*	5.11 ± 0.2	
	2002 July	k	FFA	8.99 ± 0.1	HD 9878
		PAHcs	FFA	5.90 ± 0.3	HD 9329
AFGL 2019	2000 June	CH4	annulus 36	2.48 ± 0.1	HD 163428
		h	annulus 36	3.84 ± 0.1	HD 156992
		PAHcs	annulus 36	1.52 ± 0.1	HD 163428
AFGL 2199	1998 April	CH4	annulus 36	2.99 ± 0.1	HD 170137
		PAHcs	annulus 36	1.80 ± 0.1	HD 170137
AFGL 2290	1998 June	CH4	annulus 36	4.72 ± 0.1	HD 173074
		PAHcs	annulus 36	2.60 ± 0.1	HD 173074
	1999 April	CH4	annulus 36	5.61 ± 0.1	HD 173833
		k	annulus 36	6.19 ± 0.32	HD 231437
		PAHcs	annulus 36	3.29 ± 0.1	HD 173833
CIT 1	2000 June	CH4	annulus 36	2.60 ± 0.1	λ And
		h	annulus 36	4.18 ± 0.25	HD 222499
		PAHcs	annulus 36	1.51 ± 0.1	λ And
CIT 3	1997 December	Kcont	annulus 36	1.08 ± 0.1	δ Psc
		PAHcs	annulus 36	-0.14 ± 0.1	δ Psc
	1998 September	CH4	Golay 21	2.45 ± 0.1	δ Psc
		PAHcs	Golay 21	1.04 ± 0.1	δ Psc
v1300 Aql	1998 June	CH4	annulus 36	1.39 ± 0.1	HD 189114
		h	annulus 36	3.29 ± 0.25	HD 192464
		PAHcs	annulus 36	0.60 ± 0.1	HD 189114
	1999 July	kcont	annulus 36	2.02 ± 0.1	SAO 14382
		PAHcs	annulus 36	0.86 ± 0.1	SAO 14382
AFGL 1922	2000 June	k	annulus 36	6.34 ± 0.25	HD 156992
		PAHcs	KL relation*	3.62 ± 0.25	
	2001 June	k	annulus 36	4.90 ± 0.1	HD 158774
		PAHcs	KL relation*	2.32 ± 0.25	
AFGL 1977	1998 June	CH4	annulus 36	4.19 ± 0.1	HD 158227
		h	annulus 36	7.05 ± 0.1	HD 158227
		PAHcs	annulus 36	1.84 ± 0.1	HD 157049
	1999 April	CH4	annulus 36	2.77 ± 0.1	HD 157049
		PAHcs	annulus 36	0.59 ± 0.1	HD 157049
AFGL 2135	2001 June	k	annulus 36	3.29 ± 0.1	HD 168366, HD 181700
		PAHcs	annulus 36	1.27 ± 0.3	HD 177716
AFGL 2232	1998 June	CH4	annulus 36	2.04 ± 0.1	HD 158227
		h	annulus 36	4.12 ± 0.1	HD 158227
		PAHcs	annulus 36	0.68 ± 0.1	HD 157049
		CH4	Golay 21	2.28 ± 0.3	HD 168720
		PAHcs	Golay 21	0.94 ± 0.3	HD 168720
	1999 April	CH4	annulus 36	1.06 ± 0.1	HD 173833
		PAHcs	annulus 36	-0.38 ± 0.1	HD 173833
AFGL 2513	1998 September	h	annulus 36	6.58 ± 0.1	HD 196241
		CH4	annulus 36	4.03 ± 0.1	HD 200451
		PAHcs	annulus 36	3.16 ± 0.3	ϵ Cyg
	1999 July	CH4	annulus 36	2.90 ± 0.1	HD 188947
		PAHcs	annulus 36	1.70 ± 0.1	HD 188947
AFGL 2686	1998 September	CH4	annulus 36	2.95 ± 0.1	HD 200451
		h	annulus 36	5.82 ± 0.21	HD 200451
		PAHcs	annulus 36	1.01 ± 0.1	ϵ Cyg, λ And
	1999 July	CH4	annulus 36	5.13 ± 0.1	HD 188947
		PAHcs	annulus 36	2.92 ± 0.1	HD 188947
		h	annulus 36	8.48 ± 0.3	HD 198330
AFGL 4211	2000 June	CH4	annulus 36	3.62 ± 0.3	HD 137709
		PAHcs	annulus 36	1.42 ± 0.3	HD 137709
	2001 June	k	annulus 36	4.70 ± 0.1	HD 137709
		PAHcs	KL relation*	2.64 ± 0.2	
IRAS 15148−4940	2001 June	CH4	annulus 36	1.25 ± 0.3	HD 137709
		k	annulus 36	1.30 ± 0.3	HD 137709
		PAHcs	annulus 36	1.71 ± 0.1	HD 136422

Table 3 – *continued*

Target	Date(s) (UT)	Filter	Aperture mask	Magnitude	Calibrator names
IY Hya	1999 April	CH4	annulus 36	2.08 ± 0.1	HD 87262
		PAHcs	annulus 36	1.37 ± 0.1	μ Hya
LP And	1998 September	CH4	annulus 36	3.89 ± 0.1	HD 222499, λ And
		h	annulus 36	7.05 ± 0.25	HD 222499
		PAHcs	annulus 36	1.72 ± 0.1	λ And
	1999 July	CH4	Golay 21	4.01 ± 0.1	α Cas
		PAHcs	Golay 21	1.80 ± 0.1	α Cas
	1999 January	CH4	Golay 21	3.26 ± 0.1	α Cas
		PAHcs	Golay 21	1.18 ± 0.1	α Cas
RV Aqr	1999 July	CH4	Golay 21	1.23 ± 0.25	SAO 143482, 3 Aqr
		PAHcs	Golay 21	0.56 ± 0.25	SAO 143482, 3 Aqr
	1998 June	CH4	Golay 21	1.52 ± 0.1	HD 196321
		PAHcs	Golay 21	1.15 ± 0.1	HD 196321
v1899 Cyg	1998 June	CH4	annulus 36	5.53 ± 0.1	HD 202897
		h	annulus 36	7.87 ± 0.3	HD 200817
		PAHcs	annulus 36	3.71 ± 0.1	HD 202897
	1999 July	k	annulus 36	6.40 ± 0.1	HD 198661
		PAHcs	KL relation*	4.72 ± 0.2	
V Cyg	1998 June	feii	annulus 36	2.59 ± 0.1	HD 192909
		kcont	annulus 36	0.53 ± 0.1	HD 192909
		CH4	Golay 21	0.50 ± 0.1	HD 192909
		PAHcs	annulus 36	0.26 ± 0.1	HD 192909
		PAHcs	Golay 21	0.19 ± 0.1	HD 192909
	1999 April	CH4	Golay 21	0.15 ± 0.1	ξ Cyg
		PAHcs	Golay 21	-0.25 ± 0.1	ξ Cyg
	2001 June	CH4	annulus 36	-0.27 ± 0.1	ξ Cyg
		PAHcs	annulus 36	-0.69 ± 0.1	ξ Cyg

*This point was extrapolated from another epoch for the same star and assigned an error of 0.2 mag.
Note. The horizontal line separates oxygen rich (top) from carbon rich (bottom).

taken. Occasionally no near-IR measurements were available for some calibrators and we used the calibrator spectral type and the *K*-band flux to estimate the flux density at these longer wavelengths.

As a data quality check, we compared our photometry with 2MASS and found good general agreement, although strict agreement was not expected since our targets are highly variable and there is some difference in beam sizes. We estimated the error on the photometry points at 10 per cent based on night-to-night variations. However, there were instances when we assigned larger errors (between 10 and 32 per cent) due to saturation of the 2MASS photometry used for the calibrator, intrinsic variability of the calibrator or effects of cirrus clouds in some of the original data. Indeed, there were some nights too contaminated by variable clouds to allow photometry to be extracted at all.

Table 3 is a journal of observations, including the observing date(s), the filter(s) used, the aperture mask(s) used and the calibrator star name. We have compiled the adopted calibrator properties in Table 4.

2.3 Visibility data

2.3.1 Methodology

Our group carried out aperture masking interferometry at the Keck-1 telescope from 1996 to 2005. We have published images and size measurements with (at the time) unprecedented angular resolution on topics ranging from young stellar objects, carbon stars, red supergiants and photospheric diameters of Mira variables (e.g. Monnier et al. 1999; Tuthill et al. 2000a,b; Danchi, Tuthill & Monnier 2001).

The Near Infrared Camera (NIRC) camera with the image magnifier (Matthews et al. 1996) was used in conjunction with the aperture masking hardware to create fringes at the image plane. The data frames were taken in speckle mode ($T_{\rm int} = 0.14$ s) to freeze the atmosphere. In the work presented here, multiple aperture masks and bandpass filters were employed. After flat-fielding, bad pixel correction and sky-subtraction, Fourier methods were used to extract fringe visibilities and closure phases from each frame and averaged in groups of 100 frames. Absolute calibration to account for the optical transfer function and decoherence from atmospheric seeing was performed by interleaving science observations with measurements of unresolved calibrator stars. At the end of the pipeline, the data products are purely interferometric as if obtained with a long-baseline interferometer. A full description of this experiment can be found in Tuthill et al. (2000b) and Monnier (1999), with further discussion of systematic errors in Monnier et al. (2004, 2007). All V^2 and closure phase data are available from the authors; all data products are stored in the Flexible Image Transport System (FITS)-based, optical interferometry data exchange format (OI-FITS), as described in Pauls et al. (2005).

2.3.2 Basic results

Before undertaking radiative transfer modelling, we provide the results of basic geometrical analysis of the visibility data.

Table 4. Basic properties of calibrators.

Calibrator	*J* (mag)	*H* (mag)	*K* (mag)	PAHcs (mag)	Reference
HD 168720	1.79	0.875	0.870	0.794	McWilliam & Lambert (1984), Skrutskie (2006), Neugebauer & Leighton (1969)
HD 170137	3.476	2.737	2.230	2.16	Skrutskie (2006), Neugebauer & Leighton (1969)
ϵ Cyg	0.641	0.2	0.1	0.011	Neugebauer & Leighton (1969), Ghosh et al. (1984), Price & Murdock (1983)
HD 200451	4.101	3.231	2.840	–	Skrutskie (2006), Neugebauer & Leighton (1969)
HD 231437	5.027	3.958	3.693	–	Skrutskie (2006)
HD 173833	3.488	2.647	2.1	2.02	Skrutskie (2006), Neugebauer & Leighton (1969)
HD 158227	5.626	4.984	4.812	–	Skrutskie (2006)
HD 157049	1.975	1.149	0.830	0.684	Skrutskie (2006), Neugebauer & Leighton (1969), Price & Murdock (1983)
HD 168366	5.049	4.535	4.255	–	Skrutskie (2006)
HD 181700	3.938	2.993	2.735	–	Skrutskie (2006)
SAO 143482	1.665	0.790	0.573	0.436	Skrutskie (2006), Gullixson et al. (1983)
HD 189114	3.212	2.030	1.953	1.908	Skrutskie (2006), Gosnell, Hudson & Peutter (1979)
HD 137709	2.232	1.532	1.331	1.257	Skrutskie (2006), extrapolation
HD 222499	4.641	3.804	3.627	–	Skrutskie (2006)
λ And	1.970	1.4	1.287	1.245	Johnson et al. (1966), Price & Murdock (1983), Selby et al. (1988)
HD 9878	6.631	6.730	6.698	–	Skrutskie (2006)
HD 9329	4.961	4.381	4.341	4.29	Skrutskie (2006), extrapolation
HD 156992	3.901	3.123	2.926	–	Skrutskie (2006)
HD 158774	4.403	3.451	3.138	–	Skrutskie (2006), Kawara et al. (1983)
HD 198611	3.755	2.862	2.470	–	Skrutskie (2006), Neugebauer & Leighton (1969)
HD 202987	3.859	3.067	2.82	2.75	Skrutskie (2006), Neugebauer & Leighton (1969)
3 Aqr	0.934	−0.020	−0.220	−0.338	Carter (1990)
HD 192909	1.190	–	0.180	0.101	Johnson et al. (1966), Neugebauer & Leighton (1969), Price & Murdock (1983)
ξ Cyg	0.995	0.130	−0.070	−0.150	Johnson et al. (1966), Noguchi et al. (1981)
HD 200817	4.174	3.721	3.708	–	Skrutskie (2006)
HD 192464	5.180	4.176	3.879	–	Skrutskie (2006)
α Cas	0.371	−0.191	−0.270	−0.399	Voelcker (1975), Alonso, Arribas & Martinez-Roger (1994)
μ Hya	1.216	0.506	0.37	0.28	Skrutskie (2006), Price & Murdock (1983), Johnson et al. (1966)
HD 87262	2.974	2.052	1.880	–	Skrutskie (2006), Price & Murdock (1983), Neugebauer & Leighton (1969)
HD 196321	2.128	1.361	1.21	0.984 96	Skrutskie (2006), Price & Murdock (1983), Neugebauer & Leighton (1969)
HD 136422	–	–	0.8	0.535	Price (1968), Price & Murdock (1983), Eggen (1969)
δ Psc	2.031	1.198	0.890	0.739	Skrutskie (2006), Gosnell et al. (1979)
HD 198330	4.988	4.159	3.816	–	Skrutskie (2006)
HD 188947	1.934	1.438	1.621	1.561	Noguchi et al. (1981), Elias et al. (1982), Glass (1975)
χ Cas	3.019	2.481	2.311	–	Skrutskie (2006), Neugebauer & Leighton (1969)
HD 163428	–	–	1.6	1.464	White & Wing (1978), Humphreys & Ney (1974)
HD 196241	4.19	3.620	3.090	–	Morel & Magnenat (1978), Skrutskie (2006)

The simplest representation of the data is generally a circularly symmetric Gaussian envelope, a useful model to give a characteristic size to the emission. Table 5 provides the visibility intercept, V_0 (the visibility at zero baseline), and the full width at half-maximum (FWHM) for the best fit for all data sets, including the reduced χ^2. Errors are generally dominated by systematics related to the calibration procedure (i.e. seeing variation between source and calibrator visits) and we have used the relations established in Monnier et al. (2007) to quantify our errors. In some cases, there was evidence of two components to the visibility curve and we have also fitted a slightly more complex model of a point source plus a Gaussian envelope to all epochs. Table 6 contains the best-fitting parameters of the two-component model, including the estimated fraction of light in the point source ($f_{\rm point}$) and the fraction of light in the Gaussian envelope ($f_{\rm Gauss}$).

In addition,we fitted each object with a two-dimensional Gaussian function in order to search for signs of asymmetry. Objects with observed asymmetry are marked with an asterisk in Table 5. Table 7 lists all the objects with confirmed asymmetries and we include the amount of elongation $\left(\frac{\rm FWHM_{major}}{\rm FWHM_{minor}}\right)$ and the position angle (PA; degrees east of north) of the major axis. Here we have used the spread of measured position angles between wavelength channels and epochs to estimate the PA error. We will discuss further these findings in Section 4.

3 DUST SHELL MODELLING

3.1 Introduction

The objects in our study all have spectral energy distributions that peak in the IR. Indeed, these stars are surrounded by dust shells that absorb the stellar light and then re-emit the energy in the IR. In order to extract physical characteristics of these dust shells (i.e. optical depths, temperatures, etc.), we must be able to compute how the dust will absorb, scatter and re-emit the energy from the star. We accomplish this with the radiative-transfer model DUSTY (Ivezić, Nenkova & Elitzur 1999). While DUSTY is limited to calculations in spherical symmetry, we established in the previous section that most of our objects show only mild signs of global asymmetries; however, we caution that our results will be suspect for the most asymmetric of the targets listed in Table 7. Given a small number of input parameters, DUSTY can quickly compute synthetic photometry

Table 5. Results from circularly symmetric Gaussian models.

Target	Date(s)	Filter	Aperture	V_0 (±0.05)	FWHM (mas)	χ^2/DOF
AFGL 230	1997 December	k	FFA	0.71	32 ± 3	0.23
	2002 July	k	FFA	0.54	34 ± 3	0.34
		PAHcs	FFA	0.74	33 ± 2	0.05
AFGL 2019	2000 June	CH4	annulus 36	0.96	10^{+6}_{-10}	0.31
		h	annulus 36	0.90	9 ± 4	0.65
		PAHcs	annulus 36	0.95	21 ± 3	0.27
AFGL 2199	1998 April	CH4	annulus 36	0.92	14 ± 6	0.23
		PAHcs	annulus 36	1.00	22 ± 3	0.45
AFGL 2290*	1998 June	CH4	annulus 36	0.76	22 ± 4	0.33
		PAHcs	annulus 36	0.84	27 ± 3	0.69
	1999 April	CH4	annulus 36	0.72	34 ± 3	0.39
		k	annulus 36	0.75	32 ± 3	0.51
		PAHcs	annulus 36	0.83	36 ± 2	0.36
Cit 1*	2000 June	CH4	annulus 36	0.92	15 ± 5	0.35
		h	annulus 36	0.93	14 ± 3	0.37
		PAHcs	annulus 36	0.94	20 ± 4	0.46
Cit 3*	1997 December	kcont	annulus 36	0.89	20 ± 5	0.44
		PAHcs	annulus 36	0.89	37 ± 2	0.21
	1998 September	CH4	Golay 21	0.89	21 ± 4	0.35
		PAHcs	Golay 21	0.90	29 ± 2	0.25
v1300 Aql*	1998 June	CH4	annulus 36	0.83	14 ± 6	0.43
		h	annulus 36	0.81	14 ± 3	0.41
		PAHcs	annulus 36	0.84	23 ± 3	0.50
	1999 July	kcont	annulus 36	0.87	18 ± 5	0.39
		PAHcs	annulus 36	0.90	21 ± 3	0.52
AFGL 1922	2000 June	k	annulus 36	0.76	24 ± 4	0.88
	2001 June	k	annulus 36	0.83	29 ± 4	0.76
		PAHcs	annulus 36	0.95	58 ± 2	0.43
AFGL 1977*	1998 June	CH4	annulus 36	0.78	24 ± 4	0.26
		h	annulus 36	0.76	17 ± 3	0.68
		PAHcs	annulus 36	0.94	34 ± 2	0.41
	1999 April	CH4	annulus 36	0.96	29 ± 4	0.25
		PAHcs	annulus 36	0.89	52 ± 2	0.26
AFGL 2135	2001 June	k	annulus 36	0.66	17 ± 5	0.49
	2001 June	PAHcs	annulus 36	0.50	34 ± 2	0.13
AFGL 2232*	1998 June	CH4	annulus 36	0.83	18 ± 5	1.32
		h	annulus 36	0.81	14 ± 3	0.50
		PAHcs	annulus 36	0.90	33 ± 2	0.56
		CH4	Golay 21	0.91	20 ± 5	0.17
		PAHcs	Golay 21	0.90	34 ± 2	0.14
	1999 April	CH4	annulus 36	0.69	44 ± 3	0.19
		PAHcs	annulus 36	0.86	42 ± 2	0.12
AFGL 2513*	1998 September	h	annulus 36	1.00	1^{+9}_{-1}	1.15
		CH4	annulus 36	0.94	10^{+6}_{-10}	0.18
		PAHcs	annulus 36	1.00	16 ± 4	0.70
	1999 July	CH4	annulus 36	1.00	11^{+6}_{-9}	0.32
		PAHcs	annulus 36	0.96	24 ± 3	0.36
AFGL 2686	1998 September	CH4	annulus 36	0.89	29 ± 4	0.44
		h	annulus 36	0.89	26 ± 2	0.47
		PAHcs	annulus 36	0.89	35 ± 2	0.36
	1999 July	CH4	annulus 36	0.92	26 ± 4	0.68
		PAHcs	annulus 36	0.91	33 ± 2	0.44
		h	annulus 36	0.77	28 ± 2	0.87
AFGL 4211	2000 June	CH4	annulus 36	0.78	31 ± 3	0.48
		PAHcs	annulus 36	0.82	70 ± 3	0.10
	2001 June	k	annulus 36	0.62	20 ± 5	0.63
IRAS 15148−4940	2001 June	CH4	annulus 36	0.77	13 ± 7	0.41
		k	annulus 36	0.82	13 ± 7	0.59
		PAHcs	annulus 36	0.86	25 ± 3	0.39
IY Hya	1999 April	CH4	annulus 36	0.88	14 ± 6	0.32
		PAHcs	annulus 36	0.94	33 ± 2	0.28

Table 5 – *continued*

Target	Date(s)	Filter	Aperture	V_0 (±0.05)	FWHM (mas)	χ^2/DOF
LP And*	1998 September	CH4	annulus 36	0.83	25 ± 4	0.52
		h	annulus 36	0.68	20 ± 3	0.56
		PAHcs	annulus 36	0.86	47 ± 2	0.49
	1999 July	CH4	Golay 21	0.89	24 ± 4	0.99
		PAHcs	Golay 21	0.79	48 ± 2	0.50
	1999 January	CH4	Golay 21	0.70	25 ± 4	2.41
		PAHcs	Golay 21	0.66	35 ± 2	0.45
RV Aqr*	1999 July	CH4	Golay 21	1.00	8 ± 8	0.16
		PAHcs	Golay 21	0.96	26 ± 3	0.21
	1998 June	CH4	Golay 21	0.98	12 ± 8	0.13
		PAHcs	Golay 21	1.00	27 ± 3	0.36
v1899 Cyg	1998 June	CH4	annulus 36	0.88	18 ± 5	0.35
		h	annulus 36	0.86	16 ± 3	0.39
		PAHcs	annulus 36	0.92	22 ± 3	0.32
	1999 July	k	annulus 36	0.93	15 ± 5	0.62
V Cyg	1998 June	feii	annulus 36	0.87	14 ± 3	0.92
		kcont	annulus 36	0.96	16 ± 5	1.15
		PAHcs	annulus 36	0.90	34 ± 2	0.51
		CH4	Golay 21	1.00	18 ± 5	0.35
		PAHcs	Golay 21	0.92	38 ± 2	0.10
	1999 April	CH4	Golay 21	0.93	17 ± 5	0.15
		PAHcs	Golay 21	0.86	38 ± 2	0.12
	2001 June	CH4	annulus 36	0.82	19 ± 5	0.26
		PAHcs	annulus 36	0.83	42 ± 2	0.15

*Target is asymmetric; see Table 7 for further details.
Note. The horizontal line separates oxygen rich (top) from carbon rich (bottom).

Table 6. Results from central point plus circularly symmetric Gaussian models.

Target	Date(s)	Filter	Aperture	$f_{\rm Point}$ (±0.05)	$f_{\rm Gauss}$ (±0.05)	FWHM (mas)	χ^2/DOF
AFGL 230	1997 December	k	FFA	0.24	0.52	47 ± 7	0.21
	2002 July	k	FFA	0.30	0.42	98 ± 7	0.15
		PAHcs	FFA	0.50	0.32	86 ± 8	0.42
AFGL 2019	2000 June	CH4	annulus 36	0.86	0.14	51^{+30}_{-45}	0.28
		h	annulus 36	0.00	0.83	1^{+9}_{-1}	0.83
		PAHcs	annulus 36	0.45	0.51	31 ± 5	0.27
AFGL 2199	1998 April	CH4	annulus 36	0.38	0.54	19 ± 9	0.22
		PAHcs	annulus 36	0.36	0.68	30 ± 4	0.43
AFGL 2290*	1998 June	CH4	annulus 36	0.44	0.38	46 ± 12	0.26
		PAHcs	annulus 36	0.55	0.38	68 ± 7	0.61
	1999 April	CH4	annulus 36	0.31	0.51	66 ± 9	0.21
		k	annulus 36	0.34	0.56	66 ± 9	0.31
		PAHcs	annulus 36	0.25	0.60	49 ± 3	0.35
CIT 1*	2000 June	CH4	annulus 36	0.00	0.92	14 ± 6	0.35
		h	annulus 36	0.47	0.49	23 ± 6	0.36
		PAHcs	annulus 36	0.00	0.94	20 ± 4	0.46
CIT 3*	1997 December	kcont	annulus 36	0.58	0.50	53 ± 13	0.23
		PAHcs	annulus 36	0.36	0.62	60 ± 4	0.02
	1998 September	CH4	Golay 21	0.50	0.44	40 ± 10	0.03
		PAHcs	Golay 21	0.46	0.47	50 ± 5	0.20
v1300 Aql*	1998 June	CH4	annulus 36	0.64	0.23	43 ± 20	0.40
		h	annulus 36	0.45	0.38	25 ± 7	0.39
		PAHcs	annulus 36	0.64	0.34	80 ± 10	0.30
	1999 July	kcont	annulus 36	0.00	0.87	18 ± 5	0.39
		PAHcs	annulus 36	0.17	0.73	24 ± 4	0.52
AFGL 1922	2000 June	k	annulus 36	0.42	0.39	47 ± 11	0.83
	2001 June	k	annulus 36	0.43	0.49	57 ± 12	0.62
		PAHcs	annulus 36	0.51	0.47	105 ± 6	0.41

Table 6 – *continued*

Target	Date(s)	Filter	Aperture	$f_{\rm Point}$ (±0.05)	$f_{\rm Gauss}$ (±0.05)	FWHM (mas)	χ^2/DOF
AFGL 1977*	1998 June	CH4	annulus 36	0.36	0.45	41 ± 9	0.22
		h	annulus 36	0.50	0.33	43^{+8}_{-13}	0.59
		PAHcs	annulus 36	0.42	0.58	56 ± 4	0.36
	1999 April	CH4	annulus 36	0.34	0.69	43 ± 7	0.17
		PAHcs	annulus 36	0.25	0.74	45 ± 3	0.17
AFGL 2135	2001 June	k	annulus 36	0.00	0.66	17 ± 5	0.49
	2001 June	PAHcs	annulus 36	0.28	0.27	78 ± 6	0.10
AFGL 2232*	1998 June	CH4	annulus 36	0.56	0.33	44 ± 14	0.47
		h	annulus 36	0.00	0.81	14 ± 3	1.32
		PAHcs	annulus 36	0.50	0.49	66 ± 6	0.49
		CH4	Golay 21	0.52	0.45	39 ± 10	0.10
		PAHcs	Golay 21	0.35	0.60	51 ± 4	0.09
	1999 April	CH4	annulus 36	0.23	0.56	72 ± 7	0.08
		PAHcs	annulus 36	0.26	0.64	58 ± 3	0.07
AFGL 2513*	1998 September	h	annulus 36	0.03	1.00	1^{+9}_{-1}	1.09
		CH4	annulus 36	0.81	0.14	39 ± 39	0.17
		PAHcs	annulus 36	0.03	1.00	19 ± 4	0.68
	1999 July	CH4	annulus 36	0.00	0.92	1^{+13}_{-1}	0.65
		PAHcs	annulus 36	0.67	0.37	65 ± 9	0.24
AFGL 2686	1998 September	CH4	annulus 36	0.30	0.63	42 ± 7	0.39
		h	annulus 36	0.24	0.69	35 ± 4	0.43
		PAHcs	annulus 36	0.39	0.56	58 ± 4	0.29
	1999 July	CH4	annulus 36	0.21	0.73	32 ± 5	0.67
		PAHcs	annulus 36	0.29	0.64	45 ± 3	0.42
		h	annulus 36	0.63	0.30	138^{+15}_{-9}	0.77
AFGL 4211	2000 June	CH4	annulus 36	0.36	0.54	59 ± 10	0.27
		PAHcs	annulus 36	0.16	0.70	89 ± 4	0.06
	2001 June	k	annulus 36	0.47	0.28	86^{+9}_{-19}	0.45
IRAS 15148−4940	2001 June	CH4	annulus 36	0.62	0.18	44 ± 23	0.39
		k	annulus 36	0.52	0.31	25 ± 13	0.59
		PAHcs	annulus 36	0.52	0.38	49 ± 7	0.37
IY Hya	1999 April	CH4	annulus 36	0.00	0.88	14 ± 6	0.32
		PAHcs	annulus 36	0.00	0.94	32 ± 2	0.28
LP And*	1998 September	CH4	annulus 36	0.42	0.49	49 ± 10	0.41
		h	annulus 36	0.37	0.34	39 ± 9	0.52
		PAHcs	annulus 36	0.30	0.65	74 ± 4	0.35
	1999 July	CH4	Golay 21	0.47	0.49	47 ± 11	0.91
		PAHcs	Golay 21	0.35	0.51	85 ± 5	0.42
	1999 January	CH4	Golay 21	0.47	0.49	47 ± 11	0.91
		PAHcs	Golay 21	0.35	0.51	85 ± 5	0.42
RV Aqr*	1999 July	CH4	Golay 21	0.00	0.96	1^{+13}_{-1}	0.30
		PAHcs	Golay 21	0.33	0.64	34 ± 4	0.21
	1998 June	CH4	Golay 21	0.74	0.25	30 ± 20	0.12
		PAHcs	Golay 21	0.43	0.62	42 ± 4	0.33
v1899 Cyg	1998 June	CH4	annulus 36	0.32	0.57	24 ± 7	0.35
		h	annulus 36	0.72	0.23	75 ± 15	0.30
		PAHcs	annulus 36	0.65	0.23	57 ± 13	0.31
	1999 July	k	annulus 36	0.76	0.23	52 ± 24	0.59
V Cyg	1998 June	feii	annulus 36	0.31	0.56	18 ± 5	0.91
		kcont	annulus 36	0.51	0.47	26 ± 9	1.14
		PAHcs	annulus 36	0.00	0.90	34 ± 2	0.51
		CH4	Golay 21	0.58	0.47	35 ± 10	0.30
		PAHcs	Golay 21	0.28	0.67	52 ± 3	0.06
	1999 April	CH4	Golay 21	0.52	0.43	30 ± 9	0.14
		PAHcs	Golay 21	0.31	0.60	57 ± 4	0.07
	2001 June	CH4	annulus 36	0.50	0.36	40 ± 11	0.21
		PAHcs	annulus 36	0.28	0.61	63 ± 4	0.09

*Target is asymmetric; see Table 7 for further details.

Note. The horizontal line separates oxygen rich (top) from carbon rich (bottom).

$f_{\rm Point}$ is the amount of light coming from a point source and $f_{\rm Gauss}$ is the fraction of light coming from a Gaussian envelope.

Table 7. Results from two-dimensional Gaussian models.

Target	Date(s)	Filter	$\frac{\text{FWHM}_{\text{major}}}{\text{FWHM}_{\text{minor}}}$	⟨PA⟩
AFGL 2290	1998 June	CH4	1.23	58 ± 20
		PAHcs	1.24	
	1999 April	CH4	1.24	
		k	1.24	
		PAHcs	1.06	
CIT 1	2000 June	CH4	1.13	133 ± 3
		h	1.14	
		PAHcs	1.11	
CIT 3	1997 December	Kcont	1.19	151 ± 9
		PAHcs	1.06	
	1998 September	CH4	1.28	
		PAHcs	1.04	
v1300 Aql	1998 June	CH4	1.34	108 ± 13
		h	1.14	
		PAHcs	1.19	
	1999 July	kcont	1.34	
		PAHcs	1.31	
AFGL 1977	1998 June	CH4	1.11	71 ± 18
		h	1.31	
		PAHcs	1.06	
	1999 April	CH4	1.10	
		PAHcs	1.21	
AFGL 2232	1998 June	CH4	1.37	94 ± 10
		h	1.83	
		PAHcs	1.19	
		CH4	1.10	
		PAHcs	1.08	
	1999 April	CH4	1.22	
		PAHcs	1.05	
AFGL 2513	1998 September	h	Unresolved	
		CH4	1.5	61 ± 8
		PAHcs	1.39	
	1999 July	CH4	1.38	
		PAHcs	1.2	
LP And	1998 September	CH4	1.46	108 ± 6
		h	2.03	
		PAHcs	1.39	
	1999 July	CH4	1.64	
		PAHcs	1.36	
	1999 January	CH4	1.82	
		PAHcs	1.20	
RV Aqr	1999 July	CH4	1.49	122 ± 24
		PAHcs	1.23	
	1998 June	CH4	1.35	
		PAHcs	1.22	

Sources missing from this list were found to have circularly symmetric dust shells (within errors).
Note. PA is the mean position angle of the major axis (degrees east of north) for all filters and epochs.

and intensity profiles for dust shells. These outputs can then be compared to the data that we have observationally obtained.

3.2 Model description

We applied a uniform procedure for fitting all of our objects. Here we discuss which properties were held fixed and how we explored a grid of the key dust shell parameters.

We begin with the central star. At the beginning of our study, we used a featureless Planck blackbody spectrum; however, we came to realize that a blackbody spectrum is a rather poor approximation for the extremely late-type giants in our sample due to strong molecular absorption bands. Most notably, the HCN absorption feature of carbon-rich stars sits directly at the PAHcs (3.0825 μm) wavelength, where we have many observations. Because of the severe optical absorption of the dust, spectral types are not known for most stars in our sample and we have adopted an effective temperature of 2600 K for all stars, which is as cool as we could find converged synthetic spectra. For the carbon stars, we used a MARCS model as described in Loidl, Lançon & Jørgensen (2001) and for the M-giants we used a PHOENIX NEXTGEN model as described in Hauschildt et al. (1999). The medium-resolution synthetic spectra from these sources were smoothed before input into DUSTY. Unfortunately, we do not have useful distance estimates to our sources – so we adopted a distance of 1000 pc and interstellar reddening of $E_{B-V} = 0.5$ for all objects. We note that the dust shells around the stars absorb nearly all of the energy from the central source, acting as a kind of calorimeter. Thus, while our 2600 K estimate for the central star temperature is crude, we expect the bolometric luminosity (for assumed $d = 1000$ pc) to be more accurate. However, in practice, our luminosity estimates are poor due to uncertainties in the dust shell optical depth and the fact we are not integrating the whole observed SED throughout the mid- and far-IR.

Based on the shape of the spectral energy distribution (SED) [and the presence of a silicate feature in *IRAS*-LRS (low resolution spectra)], we determined each star to have either carbon-rich dust or silicate-rich dust. Based on this assignment, we chose amorphous carbon (Hanner 1988) or warm amorphous silicates (Ossenkopf, Henning & Mathis 1992) in the DUSTY model setup. Speck, Whittington & Tartar (2008) discussed how silicates close to AB stars could quickly anneal to crystalline grains but a full exploration of optical constants for different grain types was beyond the scope of this work. For the grain size distribution, we adopted the standard MRN power-law grain size distribution between 0.005 and 0.25 μm (Mathis, Rumpl & Nordsieck 1977); a later exploration of larger grain sizes did not systematically improve fits (also see the discussion by Speck et al. 2009). Another property of the dust shell we fixed is that the dust density follows an r^{-2} power law, corresponding to constant mass-loss rate.

Lastly, we come to the parameters of the model that are not fixed: the temperature of the dust shell at the inner boundary, T_{dust}, the radius of the star, R_{star}, and the K-band optical depth $\tau_{2.2\,\mu\text{m}}$ of the dust shell (as integrated along the line of sight from the observer to the star). In the following section, we explain our fitting procedure.

3.3 Fitting methodology

We explored inner dust temperatures T_{dust} between 400 and 1500 K. This range explored both the high temperatures thought to be prohibitive of dust creation and low temperatures too cool for steady-state dust production. Note that when setting up a model in DUSTY, one does not specify the inner radius of the dust shell: this quantity is calculated based on the luminosity of the star and the specific inner shell dust temperature T_{dust}. In terms of optical depth, we explored $\tau_{2.2\,\mu\text{m}}$ between 0 and 9. This range provided a full fitting region for our objects and values of $\tau_{2.2\,\mu\text{m}}$ much above 9 were too computationally expensive. Finally, R_{star} was recognized to simply be a scaling factor for the model outputs and could easily be optimized for every pair of (T_{dust}, $\tau_{2.2\,\mu\text{m}}$). Because the DUSTY calculation was fast and we only had to optimize over a few parameters, we chose to carry out an exhaustive grid calculation over all (T_{dust}, $\tau_{2.2\,\mu\text{m}}$).

For each location in the grid, we calculated the model SED as well as the radial intensity profiles. We calculated a χ^2 based on both our coeval near-IR photometry and Keck masking visibility curves. For

Table 8. Results from the DUSTY radiative transfer model.

Target	Date(s)	$T_{\rm dust}$ (K)	$\tau_{2.2\,\mu{\rm m}}$	R_* (mas)	$L_*^{(1\,{\rm kpc})}$ (10^3 L$_\odot$)	χ^2/DOF
AFGL 230	1997 December	800^{+60}_{-90}	$4.9^{+0.9}_{-0.7}$	$1.5^{+0.5}_{-0.3}$	$4.5^{+3.1}_{-1.6}$	0.26
	2002 July	540^{+400}_{-110}	$7.4^{+1.6}_{-1.2}$	$4.1^{+4.5}_{-2.1}$	31^{+108}_{-24}	3.86
AFGL 2019	2000 June	1190^{+310}_{-250}	$0.92^{+0.23}_{-0.12}$	$3.5^{+0.7}_{-0.3}$	24^{+10}_{-4}	0.54
AFGL 2199	1998 April	1130^{+370}_{-310}	$1.6^{+1.2}_{-0.7}$	$3.3^{+2.0}_{-0.6}$	21^{+32}_{-7}	0.06
AFGL 2290	1998 June	850^{+140}_{-80}	$3.5^{+0.5}_{-0.5}$	$3.7^{+0.8}_{-0.7}$	26^{+12}_{-9}	0.33
	1999 April	800^{+140}_{-140}	$4.6^{+0.7}_{-0.5}$	$3.9^{+1.7}_{-0.8}$	29^{+31}_{-11}	2.63
CIT 1	2000 June	1190^{+310}_{-230}	$1.2^{+0.5}_{-0.2}$	$3.5^{+0.8}_{-0.4}$	24^{+12}_{-5}	0.60
CIT 3	1997 December	1110^{+230}_{-140}	$1.4^{+0.7}_{-0.5}$	$7.8^{+1.5}_{-0.6}$	116^{+49}_{-16}	0.34
	1998 September	1020^{+200}_{-110}	$1.9^{+0.7}_{-0.5}$	$5.0^{+0.8}_{-0.6}$	48^{+17}_{-11}	0.29
v1300 Aql	1998 June	1080^{+340}_{-170}	$0.92^{+0.46}_{-0.12}$	$5.8^{+1.0}_{-0.6}$	64^{+24}_{-12}	0.50
	1999 July	1160^{+340}_{-250}*	$1.60^{+0.9}_{-0.7}$*	$5.1^{+2.0}_{-0.8}$	49^{+45}_{-14}	0.11
AFGL 1922	2000 June	850^{+200}_{-60}	$5.3^{+0.7}_{-0.7}$	$4.5^{+1.1}_{-0.8}$	37^{+21}_{-13}	1.44
	2001 June	850^{+170}_{-60}	$3.9^{+0.5}_{-0.5}$	$5.2^{+1.2}_{-1.5}$	51^{+27}_{-25}	0.39
AFGL 1977	1998 June	910^{+80}_{-90}	$2.8^{+0.1}_{-0.2}$	$4.0^{+0.2}_{-0.6}$	31^{+4}_{-8}	1.69
	1999 April	990^{+90}_{-60}	$2.5^{+0.5}_{-0.2}$	$6.0^{+0.8}_{-0.4}$	68^{+19}_{-9}	0.65
AFGL 2135	2001 June	740^{+370}_{-200}	$3.2^{+4.2}_{-1.4}$	$9.4^{+65.7}_{-4.6}$	167^{+10500}_{-123}	5.04
AFGL 2232	1998 June	1110^{+140}_{-110}	$1.6^{+0.2}_{-0.2}$	$5.1^{+0.5}_{-0.5}$	48^{+11}_{-10}	0.32
	1999 April	1300^{+200}_{-230}	$2.8^{+1.4}_{-1.2}$	$9.4^{+5.0}_{-1.2}$	165^{+226}_{-41}	3.29
AFGL 2513	1998 September	1500^{+0}_{-450}	$1.9^{+0.2}_{-0.2}$	$1.7^{+0.9}_{-0.2}$	$5.3^{+7.3}_{-0.9}$	0.57
	1999 July	1110^{+400}_{-200}	$1.2^{+0.9}_{-0.5}$	$3.1^{+1.0}_{-0.4}$	18^{+14}_{-4}	0.30
AFGL 2686	1998 September	1110^{+140}_{-140}	$2.8^{+0.5}_{-0.5}$	$5.3^{+1.1}_{-0.8}$	53^{+24}_{-15}	1.85
	1999 July	820^{+60}_{-60}	$3.2^{+0.2}_{-0.2}$	$3.1^{+0.4}_{-0.3}$	19^{+4}_{-4}	1.02
AFGL 4211	2000 June	880^{+60}_{-30}	$3.7^{+0.7}_{-0.5}$	$6.7^{+0.3}_{-0.3}$	85^{+9}_{-7}	0.73
	2001 June	850^{+170}_{-80}	$4.2^{+0.9}_{-0.7}$	$6.1^{+3.7}_{-2.0}$	71^{+113}_{-39}	3.20
IRAS 15148−4940	2001 June	940^{+340}_{-170}*	$0.23^{+0.46}_{-0.12}$	$4.6^{+0.2}_{-0.9}$	40^{+4}_{-14}	2.47
IY Hya	1999 April	960^{+140}_{-110}	$0.46^{+0.46}_{-0.12}$	$4.2^{+0.1}_{-0.2}$	33^{+2}_{-3}	0.25
LP And	1998 September	880^{+70}_{-60}	$3.0^{+0.5}_{-0.2}$	$4.8^{+0.9}_{-0.5}$	43^{+19}_{-8}	1.49
	1999 July	820^{+60}_{-60}	$3.0^{+0.2}_{-0.5}$	$4.8^{+0.6}_{-0.7}$	44^{+12}_{-12}	1.00
	1999 January	880^{+90}_{-30}	$3.2^{+0.5}_{-0.2}$	$6.7^{+1.0}_{-0.7}$	85^{+27}_{-17}	1.67
RV Aqr	1999 July	1500^{+0}_{-280}	$0.46^{+0.23}_{-0.23}$	$5.4^{+0.7}_{-0.4}$	55^{+15}_{-7}	1.09
	1998 June	1190^{+310}_{-150}	$0.23^{+0.46}_{-0.12}$	$5.1^{+0.1}_{-0.7}$	48^{+2}_{-13}	0.23
v1899 Cyg	1998 June	740^{+60}_{-60}	$2.3^{+0.5}_{-0.2}$	$2.0^{+0.5}_{-0.3}$	$7.5^{+3.8}_{-1.8}$	0.53
	1999 July	600^{+340}_{-200}	$2.5^{+2.5}_{-1.2}$	$1.8^{+4.4}_{-1.0}$	$6.1^{+66}_{-4.8}$	0.12
V Cyg	1998 June	1270^{+230}_{-200}*	$0.69^{+0.46}_{-0.23}$*	$6.6^{+0.7}_{-0.1}$	83^{+19}_{-3}	3.02
	1999 April	1160^{+200}_{-110}	$0.23^{+0.23}_{-0.12}$	$9.6^{+0.3}_{-1.2}$	174^{+11}_{-40}	0.21
	2001 Jun	1270^{+140}_{-140}	$0.46^{+0.23}_{-0.23}$	$10.6^{+1.6}_{-0.6}$	212^{+70}_{-24}	0.24

*This star has two regions which meet our 1σ criteria for a best fit. The particular values shown were chosen for consistency; see the appropriate figure for more details.

Note. The horizontal line separates oxygen rich (top) from carbon rich (bottom).

the SED, we also used including V-band magnitudes in our fit with a very low weight to ensure that the optical depths were not too low (important especially when for objects without photometry in all three near-IR wavelength bands). When calculating the χ^2 for the visibility curves, we adopted the following procedure. Because the y-intercept of our observed visibility data can fluctuate ±5 per cent due to seeing calibration, we normalized each visibility to 1.0 at zero baseline before fitting. Also, we weighted the visibility points so that the SED and the visibility data were separately given equal weight in the final reduced χ^2. We purposefully chose not to include longer wavelength SED measurements, such as *IRAS* data, in our fitting. By fitting only to near-IR photometry and near-IR spatial data, we can isolate and only probe dust emitted within the last few decades. This allows us to keep the model as simple as possible and enhances the validity of our assumption of constant mass-loss rate (i.e. $\rho \propto r^{-2}$).

Once the grid calculation over inner dust temperature $T_{\rm dust}$ and $\tau_{2.2\,\mu{\rm m}}$ was completed, the χ^2 surface was used to estimate the best-fitting parameters. The uncertainty estimates were produced by considering the region where the reduced χ^2 was less than 2, a *highly conservative criterion* that reflects the highly correlated errors in our data sets. In the cases where the best-fitting χ^2 is

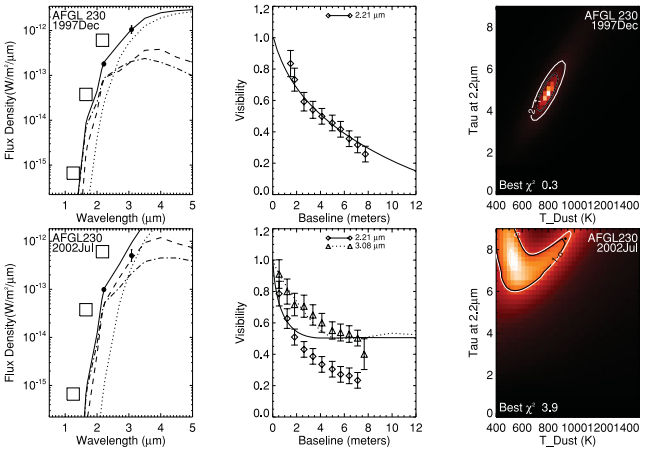

Figure 1. Best-fitting plots for AFGL230. The first row shows figures for the epoch Dec97 and the second row is for Jul02. The first panel in each row shows a fit to the SED with our new photometry included with errors (2MASS points are plotted as squares in each frame for reference). The dashed line represents the contribution from the star, the dotted line represents dust contribution, the dash–dotted line represents the contribution from scattered light and the solid line is the total flux. The second panel shows our DUSTY fits to the visibility data for each wavelength of observations. The third panel shows the χ^2/DOF surface, with bright areas showing the best-fitting region. The black contour denotes the 1σ error.

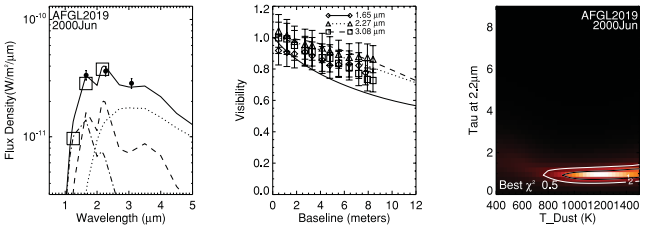

Figure 2. Best-fitting plots for AFGL2019. See the caption of Fig. 1.

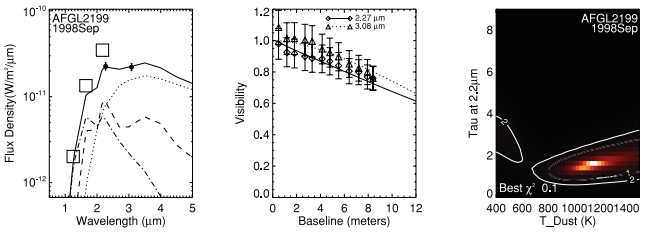

Figure 3. Best-fitting plots for AFGL2199. See the caption of Fig. 1.

above 1, we scaled the χ^2 results by the best-fitting value before estimating the parameter uncertainties. The best-fitting parameters and their uncertainties are compiled in Table 8.

In addition to providing the fitting results in a tabulated form, we also include here a series of figures which graphically represent the new data, modelling results, and the χ^2 surface in our grid. These plots can be found in each of Figs 1–20. The first panel in each figure contains the observed near-IR photometry and best-fitting model SED. The second panel in each figure contains the multi-wavelength visibility curves averaged azimuthally along with the model curves. Finally, the third panel shows the χ^2 surface in the ($T_{\rm dust}$, $\tau_{2.2\,\mu{\rm m}}$) plane. We have grouped all the epochs for the same object together so that one can see the self-consistency in the derived dust shell parameters – indeed, consistent dust shell properties were recovered when fitting to different

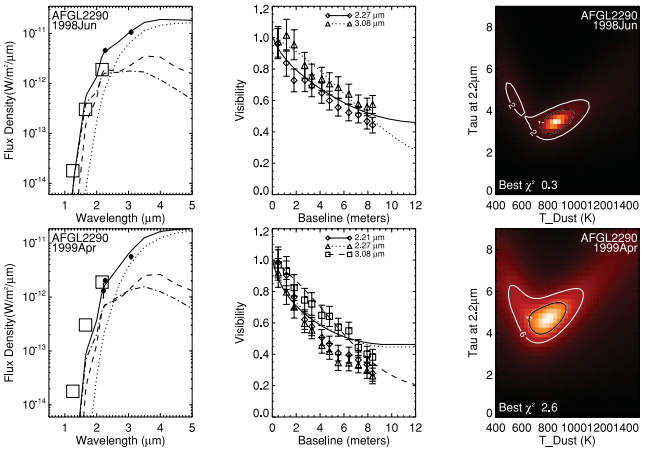

Figure 4. Best-fitting plots for AFGL2290. See the caption of Fig. 1.

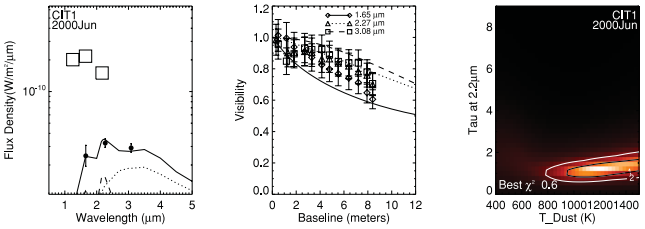

Figure 5. Best-fitting plots for CIT 1. See the caption of Fig. 1.

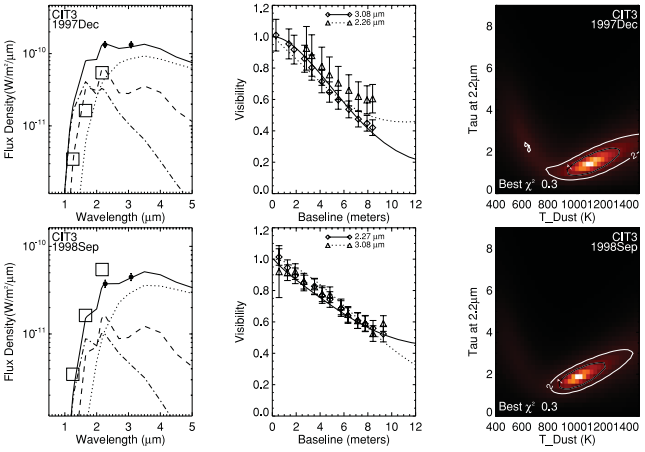

Figure 6. Best-fitting plots for CIT 3. See the caption of Fig. 1.

epochs, despite large changes in the central star luminosity due to pulsations.

One of the most important results to take away from these panels is that we clearly break the standard degeneracy between dust temperature and optical depth. This is because of our new spatial information – by measuring the *sizes* of the dust shell at various wavelengths, we can simultaneously constrain the temperature and optical depth. In the past, one typically had to choose an inner dust temperature based on physical arguments concerning the dust condensation temperatures of various dust species. Here, we see that the inner dust temperature can be constrained independently from other parameters and the implications are discussed further in the following section.

While the simultaneous fits to the near-IR SED and visibility data were generally acceptable, we found that the fits to the shortest wavelength visibility data at the *H* band were systematically worse.

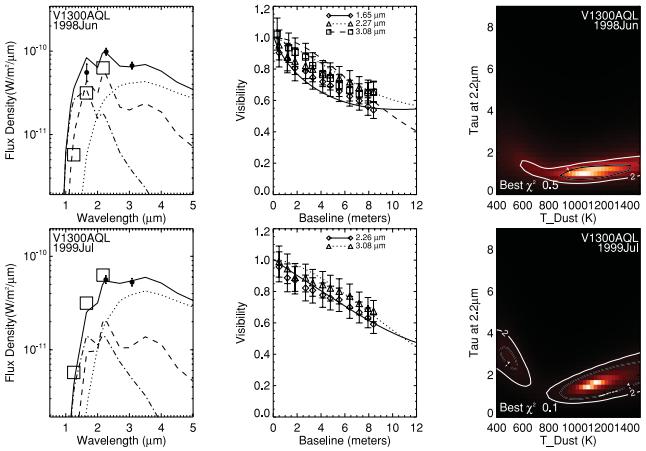

Figure 7. Best-fitting plots for v1300 Aql. See the caption of Fig. 1. For the 1999 July epoch, we chose the lower-right region as the best-fitting region because it is consistent with the best-fitting region for the 1998 June epoch.

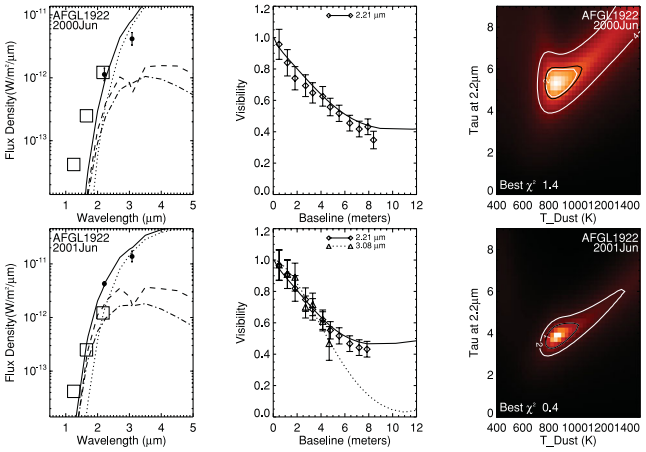

Figure 8. Best-fitting plots for AFGL1922. See the caption of Fig. 1.

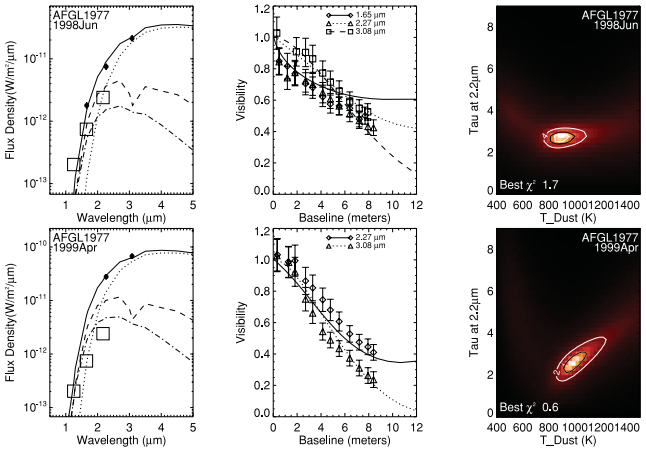

Figure 9. Best-fitting plots for AFGL1977. See the caption of Fig. 1.

Since this band is most sensitive to scattering by dust, we explored modified dust distributions, especially using larger grains; we did not find systematic improvements to the fits by altering dust size distribution from MRN or by using other dust constants.

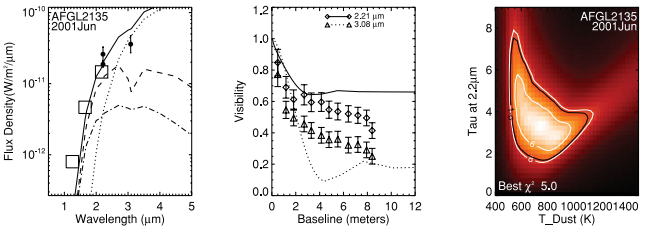

Figure 10. Best-fitting plots for AFGL2135. See the caption of Fig. 1.

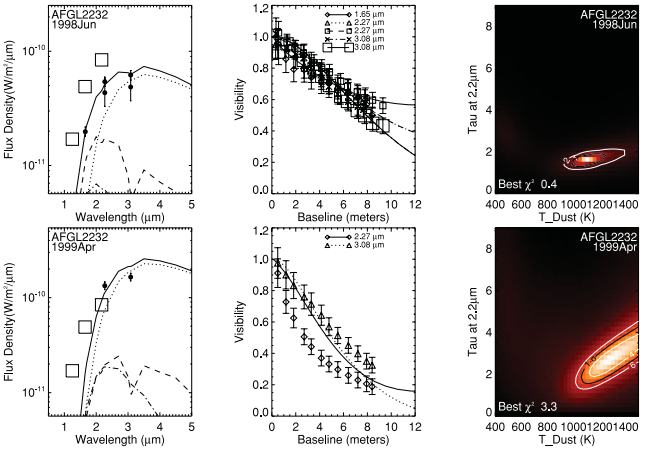

Figure 11. Best-fitting plots for AFGL2232. See the caption of Fig. 1.

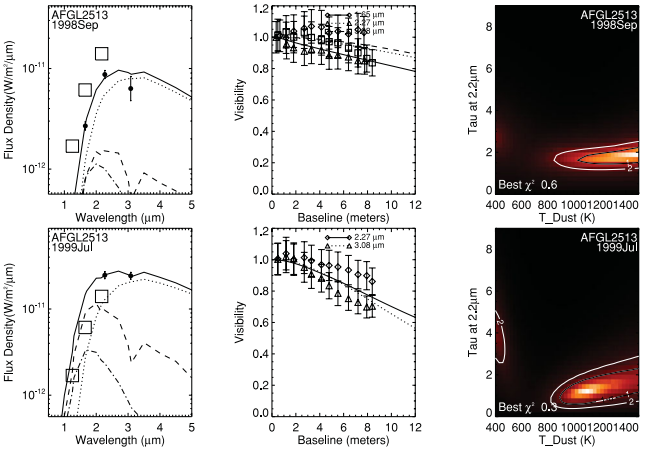

Figure 12. Best-fitting plots for AFGL2513. See the caption of Fig. 1.

4 DISCUSSION

Our survey provides the first constraints on the asymmetry of the dust shells for such a large sample of dust-enshrouded AGB stars. We found that 4 out of 7 M-stars and 5 of 13 C-stars showed evidence of dust shell asymmetries, with dust shell elongations between 10 and 40 per cent. While this level of asymmetry may sound mild, it actually (quantitatively) compares to the level of asymmetry that would be expected for the most asymmetric dust shells known if placed at 1 kpc. For instance, we know that IRC + 10216 (Tuthill et al. 2000a) and CIT 6 (Monnier, Tuthill & Danchi 2000) have dramatic global asymmetries in their dust shell, detailed imaging made possible by virtue of their proximity. If we placed these targets farther away, we would not be able to image the detail but they would appear ∼20 per cent elongated, similar to the

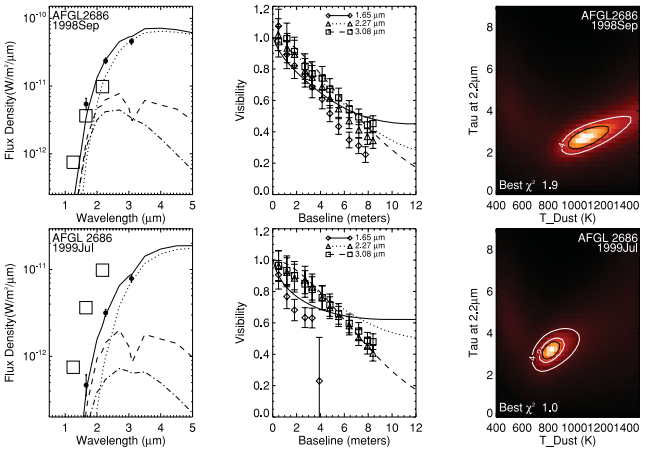

Figure 13. Best-fitting plots for AFGL2686. See the caption of Fig. 1.

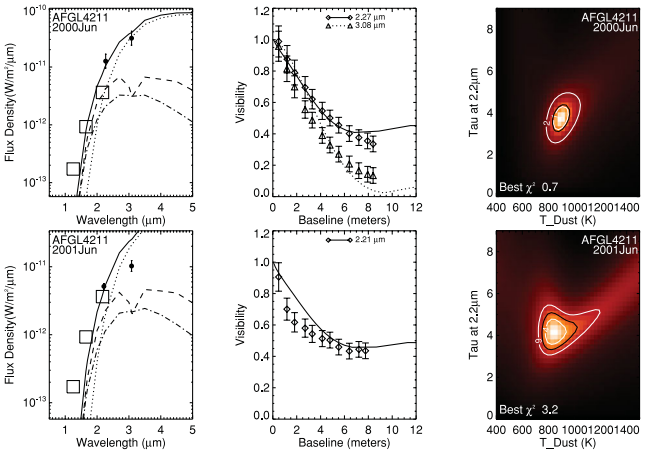

Figure 14. Best-fitting plots for AFGL4211. See the caption of Fig. 1.

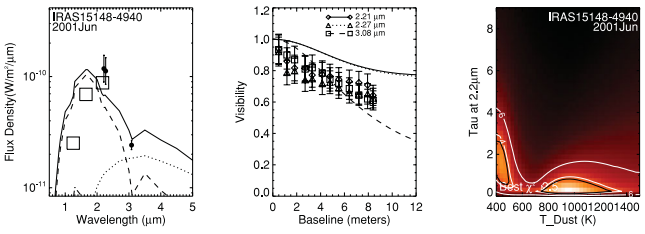

Figure 15. Best-fitting plots for IRAS15148−4940. See the caption of Fig. 1. We chose the lower-right region as the best-fitting region because in all other cases of multiple good-fitting regions, the one at low tau and high dust temperature was the consistent region.

degree observed here in 45 per cent of our sample. For CIT 3, we confirm the asymmetries seen by Hofmann et al. (2001) and note that Vinković et al. (2004) showed that the 20 per cent elongation could be explained by a bipolar outflow. That said, clumpy dust formation (Fleischer, Gauger & Sedlmayr 1992) might also cause stochastic variations in the inner dust shell geometry that could appear as short-lived elongations. Mid-IR observations with long-baseline interferometers [e.g. ISI (Infrared Spatial Interferometer), VLTI-MIDI (Very Large Telescope Interferometer-mid Infrared Interferometric Instrument)] should focus on these targets to determine the nature of the asymmetries. In addition, long-term monitoring of

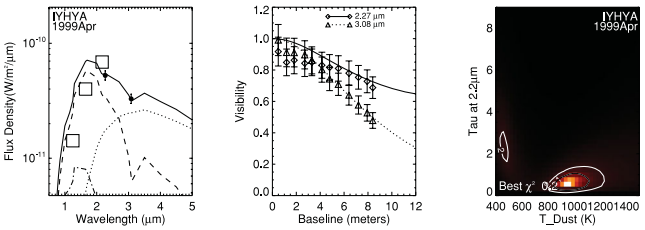

Figure 16. Best-fitting plots for IY Hya. See the caption of Fig. 1.

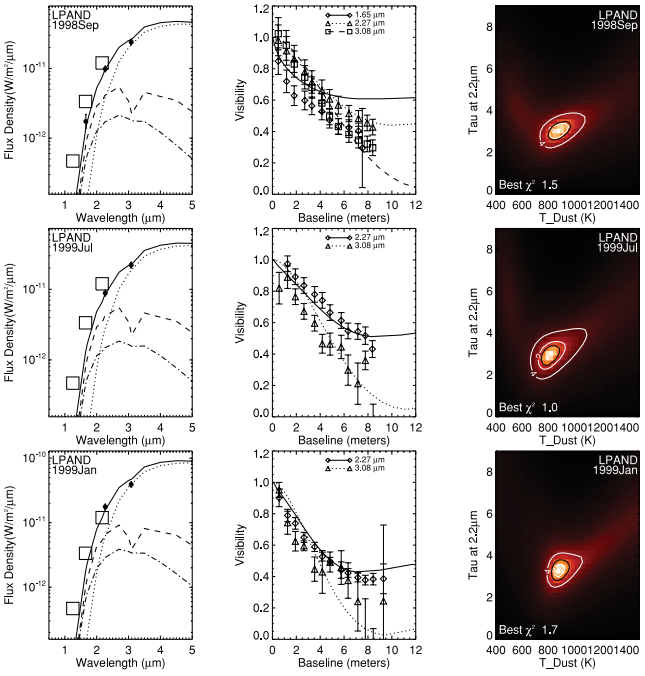

Figure 17. Best-fitting plots for LP And. See the caption of Fig. 1.

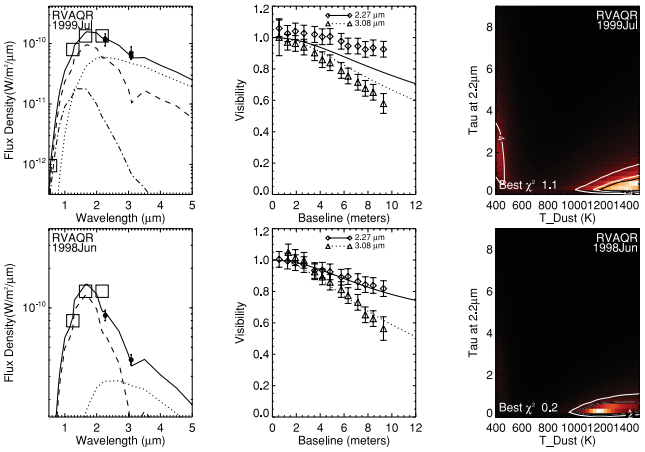

Figure 18. Best-fitting plots for RV Aqr. See the caption of Fig. 1.

these dust shells will help settle debates concerning when the environments of evolved stars develop large-scale asymmetries commonly revealed in the later planetary nebula stage. For instance, a long-term asymmetry in a constant position angle (as judged by linear polarization or spatially resolved data) would be a sign of a global bipolar mass-loss asymmetry and not just *weather*.

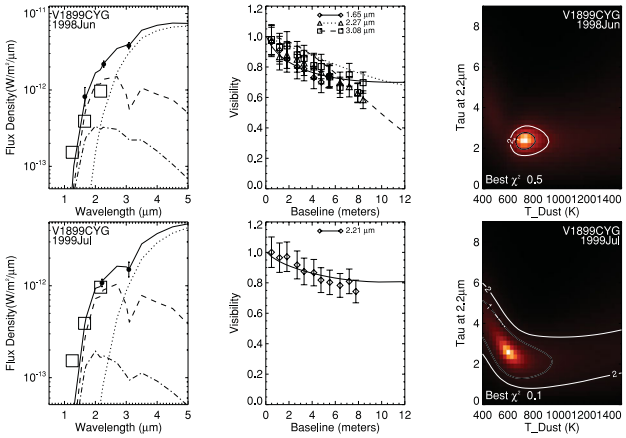

Figure 19. Best-fitting plots for v1899 Cyg. See the caption of Fig. 1.

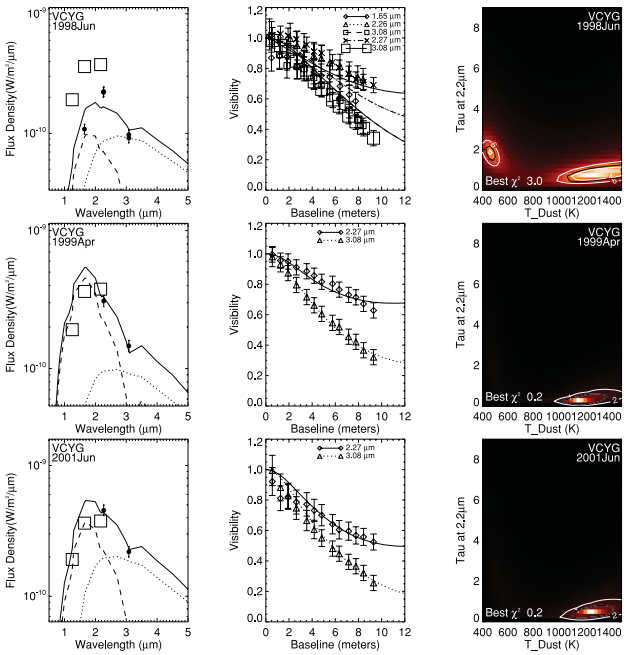

Figure 20. Best-fitting plots for V Cyg. See the caption of Fig. 1. For the 1998 June epoch, the best-fitting region was chosen to be the lower-right region because it is consistent with the other epochs.

In order to look at dust shell properties for our full sample, we have plotted the inner edge dust temperature $T_{\rm dust}$ versus total dust shell optical depth $\tau_{2.2\,\mu\rm m}$ for all our targets. Fig. 21 shows that these results split into O-rich and C-rich dust types. For *K*-band optical depths below 2, we find the sublimation temperature of $T_{\rm sub}$(silicates) $=1130\pm90$ K and $T_{\rm sub}$(amorphous carbon) $=1170\pm60$ K, both somewhat lower than expected from laboratory measurements (Lodders & Fegley 1999) and vastly below temperatures inferred from the inner edge of YSO discs ($\sim$1800 K; Tannirkulam et al. 2008; Benisty et al. 2010). One component to the observed lower dust temperature could be due to the fact that the central star varies in luminosity by about a factor of 2 during the pulsation cycle and we see the dust cooler than the condensation temperature during phases away from maximum light.

The $T_{\rm dust}$ versus optical depth $\tau_{2.2\,\mu\rm m}$ diagram (Fig. 21) also shows no statistically significant difference between O-rich and C-rich dust types, counter to expectation of higher temperatures for

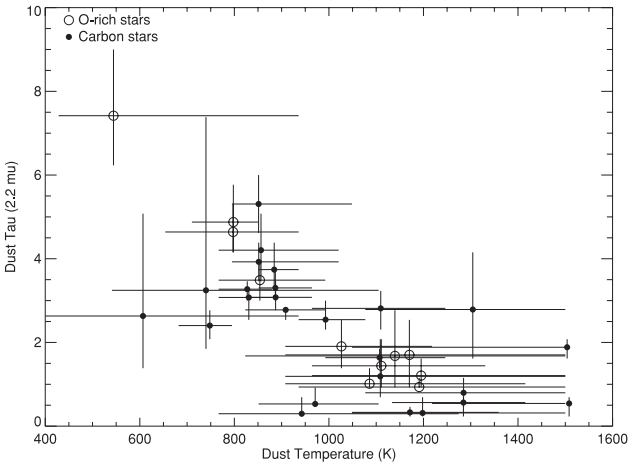

Figure 21. A plot of best fit $\tau_{2.2\,\mu\rm m}$ versus the temperature at the inner edge of the dust shell, $T_{\rm dust}$. The open symbols are used for oxygen-rich dust shells and the closed symbols are used for carbon-rich dust shells.

C-rich dust (Lodders & Fegley 1999). We recognize that our simple dust shell modelling may not lead to accurate estimates of the dust sublimation temperature if the inner dust formation environment radically departs from a power law density distribution, perhaps due to pulsations, time-scale for dust formation or multiple dust species. Interestingly though these concerns would likely affect C-rich and O-rich shells similarly and so the lack of a clear difference in sublimation temperatures between these dust types appears robust.

The other important feature of Fig. 21, $T_{\rm dust}$ versus optical depth $\tau_{2.2\,\mu\rm m}$, is that the apparent temperature at the inner edge of the dust shell gets lower and lower with increasing optical depths above 2. This appears true for both C-rich and O-rich shells. Here we do not believe we are seeing an actual reduction in the dust sublimation temperature, but rather a change in the temperature profile in the inner dust formation zone due to a breakdown in the assumption of a spherically symmetric r^{-2} density power law. We have ample evidence that dust formation is clumpy, as has been imaged in great detail for IRC + 10216 (Tuthill et al. 2000a), but these clumps have been shown to have a relatively weak effect on the temperature structure for low optical depths. Next we further explore how a clumpy dusty environment could change the temperature profile of the dust shell when the individual clumps themselves become optically thick to the stellar and even hot dust radiation field.

Clumpy structures are seen to evolve in 2D models of dust shells due to self-amplifying density perturbations (e.g. Woitke, Sedlmayr & Lopez 2000). First optically thick dust regions form and these regions cast shadows on the dust behind them. Consequently, the temperatures decrease by hundreds of kelvins and this allows for a higher rate of dust formation in these shadow regions. Scattering and re-emission of light by the optical thick regions increases the intensity of radiation between them and eventually the light escapes through the optically thin regions in between the optically thick regions. Thereupon, the temperature within the optically thin regions increases, which decreases the rate of dust production. These processes thus amplify the initial homogeneities until large-scale clumpy structures start to form, such as 'dust fingers' (Woitke & Niccolini 2005). Indeed, Woitke & Niccolini (2005) did see *average dust temperatures to be reduced* due to these opacity effects but at much weaker level than we see in Fig. 21. Realizing that our data reveal a strong effect only at τ's several times larger than probed by

Woitke & Niccolini (2005), we suggest that dust shadowing effects get dramatically stronger when individual clumps become optically thick to both stellar radiation and hot dust emission. A 3D radiative transfer calculation of a dusty dust shell could validate or disprove this explanation.

In conclusion, our large sample of spatially resolved dust-enshrouded stars have led to new insights into the late stages of AGB star evolution. We find levels of dust shell elongations that point to significant asymmetries in nearly half of our targets. Our spatial and SED data combined have eliminated some model degeneracies, and we now have the best constraints on the actual sublimation temperatures for dust forming in these outflows, finding lower temperatures than expected from terrestrial experiments and not confirming the large difference expected between carbon-rich and silicate-rich dust. Lastly, we discovered a systematic change in the temperature profile for inner-most dust regions when the dust shell optical depth rises above $\tau_{2.2\,\mu m} > 2$. This observed lowering of the central dust temperatures could be naturally explained as a consequence of shadowing caused by clumpy dust formation on spatial scales smaller than our angular resolution, but other possibilities should be further explored as well.

ACKNOWLEDGMENTS

We thank Dr Charles Townes for his long-standing support of this work. We also thank Angela Speck for her insightful comments upon reading a draft of this manuscript. We acknowledge interesting discussions with Peter Woitke regarding the effect of clumpy structures on the temperature profile, and we thank Rita Loidl Gautschy for her help in acquiring the C-star synthetic spectrum. This research has made use of the SIMBAD data base, operated at CDS, Strasbourg, France. This publication makes use of data products from the Two Micron All Sky Survey (2MASS), which is a joint project of the University of Massachusetts and the Infrared Processing and Analysis Center/California Institute of Technology, funded by the National Aeronautics and Space Administration and the National Science Foundation. The data presented herein were obtained at the W. M. Keck Observatory, which is operated as a scientific partnership among the California Institute of Technology, the University of California and the National Aeronautics and Space Administration. The Keck Observatory was made possible by the generous financial support of the W. M. Keck Foundation. We wish to recognize and acknowledge the very significant cultural role and reverence that the summit of Mauna Kea has always had within the indigenous Hawaiian community. We are most fortunate to have the opportunity to conduct observations from this mountain.

REFERENCES

Alonso A., Arribas S., Martinez-Roger C., 1994, A&A, 282, 684
Balick B., Frank A., 2002, ARA&A, 40, 439
Benisty M. et al., 2010, A&A, 511, A74
Buscombe W., 1998, VizieR On-line Data Catalog III/206 http://cdsarc.u-strasbg.fr/viz-bin/Cat?III/206
Carter B. S., 1990, MNRAS, 242, 1
Danchi W. C., Bester M., Degiacomi C. G., Greenhill L. J., Townes C. H., 1994, AJ, 107, 1469
Danchi W. C., Tuthill P. G., Monnier J. D., 2001, ApJ, 562, 440
Eggen O. J., 1969, ApJ, 158, 225
Egret D., Didelon P., Mclean B. J., Russell J. L., Turon C., 1992, A&A, 258, 217
Elias J. H., Frogel J. A., Matthews K., Neugebauer G., 1982, AJ, 87, 1029
Fleischer A. J., Gauger A., Sedlmayr E., 1992, A&A, 266, 321
Garcia-Hernandez D., Garcia-Lario P., Plez B., Manchado A., D'Antona F., Lub J., Habing H., 2007, A&A, 462, 711
Gezari D. Y., Pitts P. S., Schmitz M., 1993, Catalog of Infrared Observations (NASA Ref. Publ. 1294), NASA, Washington DC
Ghosh S., Iyengar K. V. K., Tandon S. N., Verma R. P., Daniel R. R., Rengarajan T. N., 1984, MNRAS, 206, 611
Glass I. S., 1975, MNRAS, 171, 19P
Gosnell T. R., Hudson H., Peutter R. C., 1979, AJ, 84, 538
Gullixson C., Gehrz R. D., Hackwell J. A., Grasdalen G. L., Castelaz M., 1983, ApJS, 53, 413
Haniff C. A., Buscher D. F., 1998, A&A, 334, L5
Hanner M., 1988, NASA Conf Publ. 3004. Infrared Observations of Comets Halley and Wilsen and Properties of the Grains. NASA, Washington, DC, p. 77
Hauschildt P. H., Allard F., Ferguson J., Baron E., Alexander D. R., 1999, ApJ, 525, 871
Hofmann K.-H., Balega Y., Blöcker T., Weigelt G., 2001, A&A, 379, 529
Humphreys R. M., Ney R. P., 1974, ApJ, 194, 623
Ivezic Z., Elitzur M., 1995, ApJ, 445, 415
Ivezić Z., Nenkova M., Elitzur M., 1999, Univ. Kentucky Internal Rep. http://www.pa.uky.edu/moshe/dusty
Johnson H. L., Iriarte B., Mitchell R. I., Wisniewskj W. Z., 1966, Commun. Lunar Plan. Lab., 4
Kawara K., Kozasa T., Sato S., Okuda H., Kobayashi Y., Jugaku J., 1983, Kyoto Univ. Mem. Fac. Sci., Kyoto Univ., Ser. A Phys. Astrophys. Geophys. Chem., 36, 353
Lodders K., Fegley B., Jr, 1999, in Le Bertre T., Lebre A., Waelkens C., eds, IAU Symp., 191, Asymptotic Giant Branch Stars, Springer, New York, NY, p 279
Loidl R., Lançon A., Jørgensen U. G., 2001, A&A, 371, 1065
Mathis J. S., Rumpl W., Nordsieck K. H., 1977, ApJ, 217, 425
Matthews K., Ghez A. M., Weinberger A. J., Neugebauer G., 1996, PASP, 108, 615
McWilliam A., Lambert D. L., 1984, PASP, 96, 882
Men'shchikov A. B., Hofmann K., Weigelt G., 2002, A&A, 392, 921
Monet D. G., 1998, BAAS, 30, 1427
Monnier J. D., 1999, PhD thesis, University of California, Berkeley, CA
Monnier J. D., Tuthill P. G., Lopez B., Cruzalebes P., Danchi W. C., Haniff C. A., 1999, ApJ, 512, 351
Monnier J. D., Tuthill P. G., Danchi W. C., 2000, ApJ, 545, 957
Monnier J. D., Tuthill P. G., Danchi W. C., Murphy N., Harries T. J., 2007, ApJ, 655, 1033
Monnier J. D. et al., 2004, ApJ, 605, 436
Morel M., Magnenat P., 1978, A&A, 34
Neugebauer G., Leighton R. B., 1969, NASA Special Publ. 477, NASA, Washington DC
Noguchi K., Kawara K., Kobayashi Y., Okuda H., Sato S., Oishi M., 1981, PASJ, 33, 373
Olnon F. M. et al., 1986, A&AS, 65, 607
Ossenkopf V., Henning T., Mathis J. S., 1992, A&A, 261, 567
Pauls T. A., Young J. S., Cotton W. D., Monnier J. D., 2005, PASP, 117, 1255
Price S. D., 1968, AJ, 73, 431
Price S. D., Murdock T. L., 1983, VizieR On-line Catalog II/94, http://vizier.u-strasbg.fr/viz-bin/VizieR-3
Rowan-Robinson M., Harris S., 1982, MNRAS, 200, 197
Rowan-Robinson M., Harris S., 1983a, MNRAS, 202, 797
Rowan-Robinson M., Harris S., 1983b, MNRAS, 202, 767
Selby M. J., Hepburn I., Blackwell D. E., Booth A. J., Haddock D. J., Arribas S., Leggett S. K., Mountain C. M., 1988, A&AS, 74, 127
Skiff B., 2009, VizieR On-line Data Catalog B/mk, http://vizier.u-strasbg.fr/viz-bin/VizieR-2
Skrutskie M. F. et al., 2006, AJ, 131, 1163
Speck A. K., Whittington A. G., Tartar J. B., 2008, ApJ, 687, L91
Speck A. K., Corman A. B., Wakeman K., Wheeler C. H., Thompson G., 2009, ApJ, 691, 1202
Tannirkulam A. et al., 2008, ApJ, 689, 513
Tuthill P. G., Monnier J. D., Danchi W. C., Lopez B., 2000a, ApJ, 543, 284

Tuthill P. G., Monnier J. D., Danchi W. C., Wishnow E. H., Haniff C. A., 2000b, PASP, 112, 555
Vinković D., Blöcker T., Hofmann K.-H., Elitzur M., Weigelt G., 2004, MNRAS, 352, 852
Voelcker K., 1975, A&AS, 22, 1
Weigelt G., Balega Y., Bloecker T., Fleischer A. J., Osterbart R., Winters J. M., 1998, A&A, 333, L51
White N. M., Wing R. F., 1978, ApJ, 222, 209
Woitke P., Niccolini G., 2005, A&A, 433, 1101
Woitke P., Sedlmayr E., Lopez B., 2000, A&A, 358, 665

This paper has been typeset from a TEX/LATEX file prepared by the author.